Neutron scattering study of antiferromagnetic correlations in the Kondo semiconductor CeNiSn

1995 J. Phys.: Condens. Matter 7 8009

(http://iopscience.iop.org/0953-8984/7/41/010)

J. Phys.: Condens. Matter 7 (1995) 8009–8026. Printed in the UK

Neutron scattering study of antiferromagnetic correlations in the Kondo semiconductor CeNiSn

Taku J Sato†, Hiroaki Kadowaki†, Hideki Yoshizawa†, Toshikazu Ekino‡, Toshiro Takabatake‡¶, Hironobu Fujii‡, L P Regnault§ and Yosikazu Isikawa‖

† Institute for Solid State Physics, University of Tokyo, Roppongi, Minato-ku, Tokyo 106, Japan
‡ Faculty of Integrated Arts and Sciences, Hiroshima University, Higashi-Hiroshima 724, Japan
§ CEA–Département de Recherches Fondamentales sur la Matière Condensée, SPSMS/MDN, Centre d'Etudes Nucléaires, 38054 Grenoble Cédex 9, France
‖ Faculty of Science, Toyama University, Toyama 930, Japan

Received 26 May 1995

Abstract. Spin excitations in the Kondo semiconductor CeNiSn have been studied in a wide Q-range and in the energy range of $\hbar\omega = 1.2-7$ meV by means of single-crystal neutron scattering. The magnetic fluctuation at low temperatures in this energy range is dominated by the easy a-axis component $\mathrm{Im}\,\chi^{aa}$. Below the coherence temperature of 20 K, two dynamic antiferromagnetic correlations develop as excitation peaks at $\hbar\omega = 2$ and 4 meV. The 4 meV excitation appears at $Q = (Q_a, \frac{1}{2} + n, Q_c)$ where Q_a and Q_c are arbitrary and n is an integer, which indicates that the correlation is quasi-one dimensional along the b-axis. The 2 meV excitation appears around $Q = (0, 0, 1)$ and $(0, 1, 0)$, which shows three-dimensional Q-dependence. These two excitations reflect the nature of the Kondo coherent state of CeNiSn.

1. Introduction

Heavy-fermion or valence-fluctuation compounds exhibit a wide variety of ground states. Most of them show metallic ground states, which are paramagnetic, antiferromagnetic or superconducting. However, there are several exceptions which show insulating or semiconducting ground states exhibiting gaps or pseudogaps in electronic excitation spectra, so called Kondo insulators [1]. The mechanism of the gap formation has been intensively investigated theoretically and experimentally. CeNiSn [2, 3] and CeRhSb [4] attract special attention because of their very small pseudogaps of a few K, which are an order smaller than those of other insulating compounds, for example, SmB_6 [5], YbB_{12} [6] and $Ce_3Bi_4Pt_3$ [7].

Since large single crystals can be grown, CeNiSn has been extensively studied on its thermal, transport and magnetic properties. CeNiSn crystallizes in the orthorhombic ϵ-TiNiSn structure [8]. From the temperature dependence of specific heat, magnetic susceptibility and thermoelectric power, Takabatake *et al* [2, 3] inferred that the pseudogap with a gap energy $T_\Delta = 6$ K is formed in the Kondo coherent state with an onset temperature $T_{coh} = 12$–20 K. The magnetic susceptibility along the a-axis, which is larger than those along the b- and c-axes, and the thermoelectric power show peaks at T_{coh}. The Kondo

¶ Present address: Faculty of Science, Hiroshima University.

0953-8984/95/418009+18$19.50

coherence is also manifested in the increase of C_m/T at low temperatures, where C_m is the magnetic contribution of the specific heat, reaching 0.19 J mol^{-1} K^{-2} at T_Δ, the value of which indicates that CeNiSn is a moderately heavy-fermion system like $CeRu_2Si_2$ [9]. As the temperature is further lowered below T_Δ, C_m/T shows a strong decrease, implying the opening of the pseudogap. The pseudogap formation in the spin excitation was observed in the measurement of the temperature dependence of the nuclear spin relaxation rate $1/T_1$ of ^{119}Sn as deviation from T_1T = constant. Below T_Δ, $1/T_1$ varies as T^3. This temperature dependence led Kyogaku *et al* to propose the V-shaped state density centred at the Fermi level [10, 11].

To study the spin excitation of CeNiSn, several neutron scattering experiments were performed on polycrystalline and single-crystal samples. For high energy transfers $\hbar\omega$ up to 60 meV, experiments on polycrystalline samples showed that the spectral weight $\mathrm{Im}\,\chi(\hbar\omega)/\hbar\omega$ can be fitted by a broad quasi-elastic Lorentzian curve with Γ = 2–4 meV half width at half maximum (HWHM), and no inelastic peak originating from a crystal-field excitation was observed [12, 13, 14]. This does not rule out the presence of a crystal field, which should split the $J = \frac{5}{2}$ multiplet into three doublets. In fact, the crystal field results in anisotropy in uniform and dynamic magnetic susceptibility. A pseudogap spectrum corresponding to T_Δ was sought on a polycrystalline sample in energy transfers down to $\hbar\omega$ = 0.8 meV [14]. However, the spectral weight $\mathrm{Im}\,\chi(\hbar\omega)/\hbar\omega$ does not show any pseudogap behaviour in low $\hbar\omega$, where a strong decrease of the spectral weight is expected. The pseudogap should appear in an energy range lower than 0.8 meV, and remains to be studied.

Two groups of investigators have performed neutron scattering experiments on single crystals in an energy range $\hbar\omega$ = 1–7 meV. The spin excitation at a general wave number Q in the reciprocal space has the broad quasi-elastic features as observed in experiments on polycrystalline samples. Among these featureless spectra, the single-crystal experiments showed that there are two excitation peaks localized in Q space. Mason *et al* [15] found that an excitation peak at $\hbar\omega$ = 2 meV around $Q = (0, 0, 1)$ develops below T_{coh} in measuring the $(h, 0, l)$ scattering plane. Recently Kadowaki *et al* [16] measured the $(h, k, 0)$ and $(0, k, l)$ scattering planes, and found that a stronger excitation peak at $\hbar\omega$ = 4 meV around $Q = (Q_a, \frac{1}{2}, Q_c)$, for arbitrary Q_a and Q_c, also evolves below T_{coh}. We note that the presence of two magnetic fluctuations with peaks at non-equivalent wave numbers has been observed in the metallic Kondo compounds $CeCu_6$ and $CeRu_2Si_2$ [17]. The wave-number dependence of these excitations shows that the 2 and 4 meV excitations can be regarded as three-dimensional and quasi-one-dimensional dynamic antiferromagnetic correlations, respectively. Since the excitation energies are of the same order as k_BT_{coh}, we think that both the excitations are related to the formation of the Kondo coherence but not directly to the pseudogap observed in bulk properties. However, it should be noted that there may be an alternative viewpoint in which the two excitations are nothing but the pseudogap which is Q dependent, because the spectral weight at $Q = (0, 0, 1)$ and $(0, \frac{1}{2}, 0)$ shows the pseudogap-type behaviour. Irrespective of these viewpoints, the quasi-one-dimensional character and the pseudogap-type spectral weight of the excitations are quite unique to CeNiSn, and such a spectrum has not been observed in any other heavy-fermion or valence-fluctuation compounds. Thus these features will be a clue to clarifying the origin of the gap formation.

In this report, we present extended data of the inelastic neutron scattering experiments in a wide Q-range of the $(h, k, 0)$, (h, k, h) and $(0, k, l)$ scattering planes. We will pay attention to the anisotropy of magnetic fluctuation and related crystal field. Constant-Q scans at various wave numbers are shown in absolute units in the hope that they will be

quantitatively accounted for in future. Some of the data have been published in a brief report [16].

2. Experimental procedure

The single-crystal sample was grown by the Czochralski method [18] using a tungsten crucible in an induction furnace under an argon gas atmosphere of 5 Torr. The pulling speed was 10 mm h^{-1} and the rotation speed 5 rpm. The purities of the starting materials Ce, Ni and Sn were 99.99, 99.99 and 99.999%, respectively. The growth direction was nearly parallel to the b-axis. The crystal was 0.9 cc in volume.

Inelastic neutron scattering experiments were performed on the ISSP triple-axis spectrometer 4G-TAS installed at JRR-3M JAERI (Tokai). A pyrolytic graphite (002) reflection was used for the vertically focusing monochromator and analyser. Neutrons with higher-order wave-lengths were removed by a pyrolytic graphite filter. The experiments were carried out in either the E_i- or E_f-fixed mode with the fixed energy of 13.7 meV. For most of the scans, collimations 30′–40′–40′–80′ were employed. The energy resolution of the configuration with $E_f = 13.7$ meV was 0.9 and 1.1 meV (full width at half maximum, FWHM) at $\hbar\omega = 0$ and 4 meV, respectively. Scans requiring a high energy resolution were performed with the E_i-fixed mode, $E_i = 13.7$ meV, and the collimations 20′–40′–40′–40′. This configuration gives an energy resolution of 0.4 meV (FWHM) at $\hbar\omega = 4$ meV. The sample was mounted in a liquid ^{3}He cryostat, a closed-cycle ^{4}He refrigerator, or an Orange cryostat with the [100], [001] or [10$\bar{1}$] direction vertical so as to measure the scattering in the $(0, k, l)$, $(h, k, 0)$ or (h, k, h) scattering plane.

Inelastic neutron scattering spectra are corrected for background and absorption, and are scaled to absolute units of cross-section. They are given as the scattering function $S(Q, \hbar\omega) = (k_i/k_f)(\mathrm{d}^2\sigma/\mathrm{d}\Omega\,\mathrm{d}E_f)$. The absorption was corrected by absorption factors calculated by numerical integration. The scattering intensity was converted to absolute units by a calibration using a comparison between calculated and observed intensity of the acoustic phonon of the standard copper crystal. The volume of the CeNiSn crystal was estimated by measuring the intensity of the acoustic phonon around $Q = (0, 2, 0)$ and by comparing it to the formula of the phonon cross-section valid in the $\hbar\omega \to 0$ limit [19]. It is consistent with the volume estimated from the weight of the sample within 5%.

For the background correction, we considered four possibilities: (I) scattering by air, the cryostat and the sample holder; (II) a tail of the incoherent elastic scattering; (III) the incoherent inelastic scattering by the phonon; (IV) double scattering due to the coherent phonon and the incoherent elastic scattering. The first background (I) was measured as the scattering intensity under the same experimental conditions without the sample. The second background (II) was measured using a vanadium standard under the same spectrometer configuration. The third and fourth backgrounds (III) and (IV) were calculated numerically, where the phonon scattering cross-section was approximated by the acoustic approximation. Backgrounds (III) and (IV) were far smaller than the observed intensity, and thus were neglected. An example of these four backgrounds and a spectrum of a constant-Q scan taken at $Q = (0, \frac{3}{2}, 0)$ and $T = 2$ K are shown in figure 1. One can see that the observed spectrum has a sufficient signal-to-noise ratio. Since all conceivable backgrounds are subtracted from the data, we think that the corrected data contain the magnetic excitation and the coherent inelastic scattering by the phonon.

The coherent phonon scattering appears as peaks in inelastic spectra. In all the data shown in this report, the phonon peaks exist in an energy range above 5 meV and do not cause serious contamination to the magnetic excitation. To distinguish these phonon

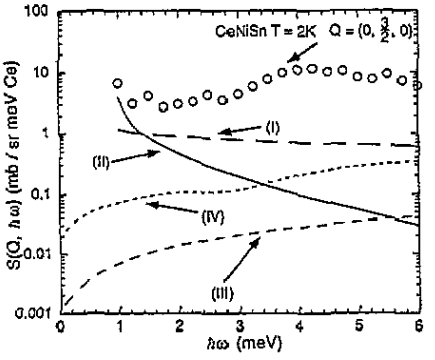

Figure 1. Example of constant-Q scan and four backgrounds. The open circle stands for the constant-Q spectrum, which is not corrected for background, at $Q = (0, \frac{3}{2}, 0)$ and $T = 2$ K. The four lines represent the backgrounds: (I) scattering by air, cryostats and sample holders; (II) a tail of the incoherent elastic scattering; (III) the incoherent inelastic scattering by the phonon; (IV) double scattering due to the coherent phonon and the incoherent elastic scattering.

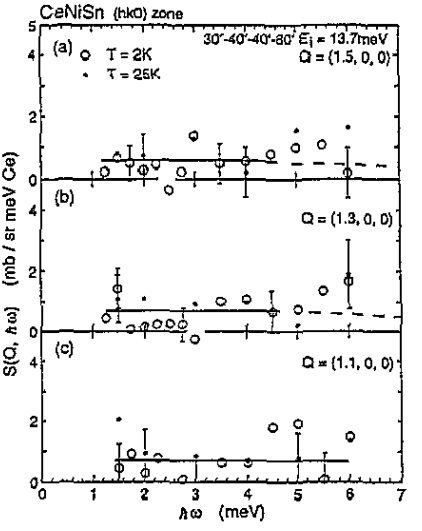

Figure 2. Constant-Q scan on the a^*-axis at $Q = (Q_a, 0, 0)$, $Q_a = \frac{3}{2}$, 1.3 and 1.1. Open and closed circles stand for data taken at $T = 2$ ($< T_{coh}$) and 25 K ($> T_{coh}$), respectively. Broken line represents magnetic contribution in which phonon scattering is subtracted. Solid line is guide to the eye.

peaks from the magnetic scattering, we used the difference of the temperature dependence between the phonon and the magnetic scattering. The phonon intensity shows the strong temperature variation due to the Bose factor $(1 + n(\hbar\omega)) = 1/(1 - e^{-\beta\hbar\omega})$, whereas the magnetic scattering has negligibly small temperature dependence. The estimated magnetic contribution will be shown by broken lines in the excitation spectra in the next section.

3. Experimental results

The scattering function of the magnetic excitation can be written using the magnetization operator $M(r, t)$ as a pair correlation function

$$S(Q, \hbar\omega) = \sum_{\alpha\beta}(\delta_{\alpha\beta} - \hat{Q}_\alpha \hat{Q}_\beta) S^{\alpha\beta}(Q, \hbar\omega) \tag{1}$$

$$S^{\alpha\beta}(Q, \hbar\omega) = \frac{(\gamma r_0)^2}{(2\mu_B)^2 (2\pi\hbar)} \int_{-\infty}^{\infty} dt\, e^{-i\omega t} \langle M_Q^\alpha M_{-Q}^\beta(t) \rangle \tag{2}$$

$$\hat{Q} = \frac{Q}{Q} \qquad M_Q^\alpha(t) = \int dr \exp(-iQ \cdot r) M^\alpha(r, t)$$

where γ and r_0 are the gyromagnetic ratio of a neutron and the classical electron radius, respectively. Alternatively the scattering function is expressed using the generalized

susceptibility.

$$S(\boldsymbol{Q},\hbar\omega)=\frac{(\gamma r_0)^2V}{(2\mu_B)^2\pi}\frac{1}{1-\exp(-\beta\hbar\omega)}\sum_{\alpha\beta}(\delta_{\alpha\beta}-\hat{Q}_\alpha\hat{Q}_\beta)\mathrm{Im}[\chi^{\alpha\beta}(\boldsymbol{Q},\hbar\omega)] \tag{3}$$

$$\chi^{\alpha\beta}(\boldsymbol{Q},\hbar\omega)-\chi^{\beta\alpha}(\boldsymbol{Q},\hbar\omega)^*=\frac{\mathrm{i}2\pi(2\mu_B)^2}{(\gamma r_0)^2V}S^{\alpha\beta}(\boldsymbol{Q},\hbar\omega)(1-\mathrm{e}^{-\beta\hbar\omega}) \tag{4}$$

where V stands for the volume of the sample. Equation (3) is also utilized to evaluate the wave-number-dependent susceptibility $\chi^{\alpha\beta}(\boldsymbol{Q})$ by the Kramers–Kronig relation

$$\chi^{\alpha\beta}(\boldsymbol{Q})=2\int_0^\infty\frac{\mathrm{d}\omega}{\pi}\frac{\mathrm{Im}[\chi^{\alpha\beta}(\boldsymbol{Q},\hbar\omega)]}{\omega}. \tag{5}$$

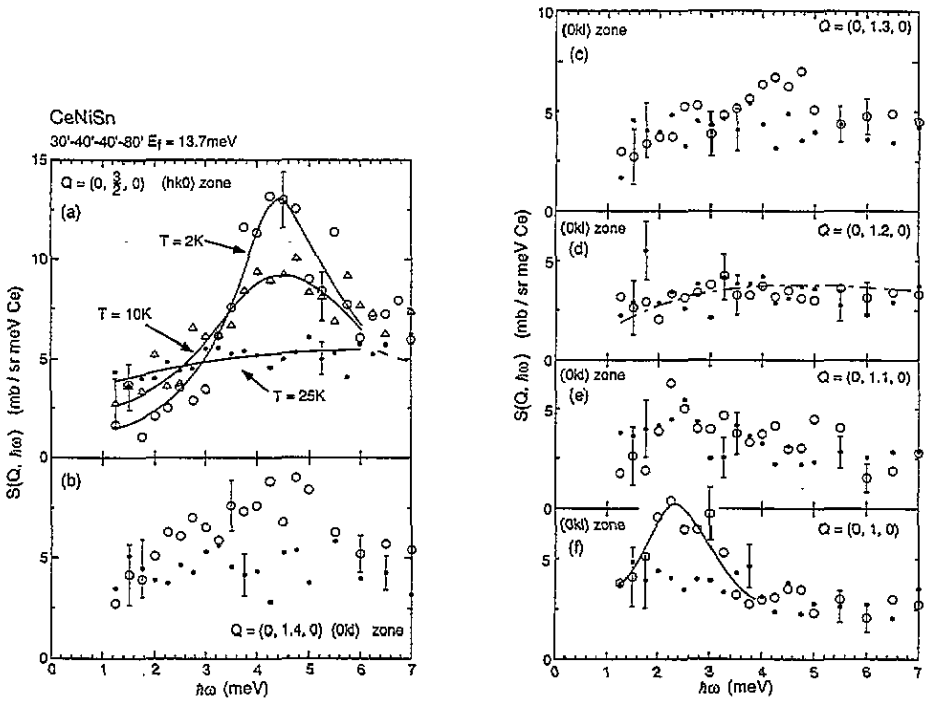

Figure 3. Constant-Q scan on the b^*-axis at $\boldsymbol{Q}=(0,Q_b,0)$, $Q_b=\frac{3}{2}$, 1.4, 1.3, 1.2, 1.1 and 1. Open circle, triangle and closed circle denote data taken at $T=2$, 15 and 25 K, respectively. The solid line is a guide to the eye. The broken line in (a) stands for phonon-subtracted magnetic contribution. The dashed-and-dotted line in (d) is a fit of the Lorentzian function to data at $T=2$ K, which is described in section 4.4.

3.1. Spectra on the a^*-, b^*- and c^*-axes

When $\boldsymbol{Q}$ is along the a^*-, b^*- or c^*-axis, equation (3) becomes simple,

$$S(\boldsymbol{Q},\hbar\omega)\propto\begin{cases}\mathrm{Im}[\chi^{bb}(\boldsymbol{Q},\hbar\omega)+\chi^{cc}(\boldsymbol{Q},\hbar\omega)] & \text{for } \boldsymbol{Q}=(Q_a,0,0)\\ \mathrm{Im}[\chi^{cc}(\boldsymbol{Q},\hbar\omega)+\chi^{aa}(\boldsymbol{Q},\hbar\omega)] & \text{for } \boldsymbol{Q}=(0,Q_b,0)\\ \mathrm{Im}[\chi^{aa}(\boldsymbol{Q},\hbar\omega)+\chi^{bb}(\boldsymbol{Q},\hbar\omega)] & \text{for } \boldsymbol{Q}=(0,0,Q_c).\end{cases} \tag{6}$$

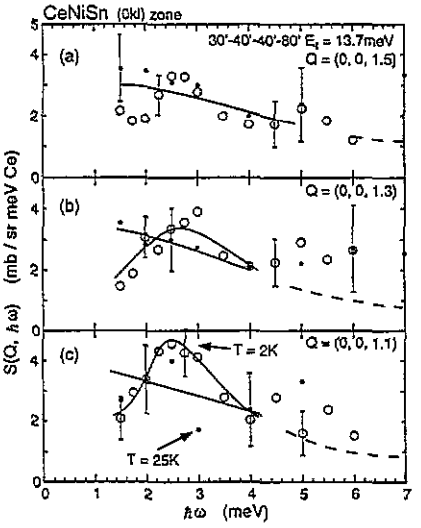

Figure 4. Constant-Q scan on the c^*-axis at $Q = (0, 0, Q_c)$, $Q_c = \frac{3}{2}$, 1.3 and 1.1. The open and closed circles stand for data taken at $T = 2$ and 25 K, respectively. The solid and broken lines are a guide to the eye and phonon-subtracted magnetic contribution, respectively.

It is worth noting that the three diagonal elements of $\mathrm{Im}\,\chi^{\alpha\alpha}(Q, \hbar\omega)$ are real and positive,

$$\mathrm{Im}[\chi^{aa}(Q, \hbar\omega)],\ \mathrm{Im}[\chi^{bb}(Q, \hbar\omega)],\ \mathrm{Im}[\chi^{cc}(Q, \hbar\omega)] \geqslant 0 \tag{7}$$

for any Q and $\hbar\omega \geqslant 0$. Spectra of several constant-Q scans on the three axes are shown in figures 2, 3 and 4. From these figures one can see three characteristics. Firstly, the spectra on the a^*-axis are much smaller than those on the b^*- and c^*-axes. If the Q dependence of the magnetic excitation is neglected, this feature means that $\mathrm{Im}\,\chi^{bb}(Q, \hbar\omega)$, $\mathrm{Im}\,\chi^{cc}(Q, \hbar\omega) \ll \mathrm{Im}\,\chi^{aa}(Q, \hbar\omega)$, that is, the magnetic fluctuation is restricted along the easy a-axis. Secondly, there are the two Q-dependent magnetic excitations at $\hbar\omega = 2$ and 4 meV. The 2 meV excitation appears at $Q = (0, 0, 1)$ and $(0, 1, 0)$, whereas the 4 meV excitation at $Q = (0, \frac{3}{2}, 0)$. Thirdly, at general Q magnetic excitation spectra are flat and featureless, as observed on polycrystalline samples. This Q-independent part is often referred to as the single-site contribution. In the subsequent subsections, we will show more detailed data on these characteristics.

3.2. Anisotropy of the magnetic fluctuation

The anisotropy of the magnetic fluctuation, $\mathrm{Im}\,\chi^{\alpha\alpha}(Q, \hbar\omega)$, is connected to that of the Q-dependent susceptibility, $\chi^{\alpha\alpha}(Q)$, by equation (5). $\chi^{\alpha\alpha}(Q)$ can be compared to the uniform susceptibility χ_α. We carried out the integration of equation (5) for the constant-Q scans of figures 2, 3 and 4, which give $\chi^{bb}(Q) + \chi^{cc}(Q)$, $\chi^{cc}(Q) + \chi^{aa}(Q)$ and $\chi^{aa}(Q) + \chi^{bb}(Q)$, respectively. The resultant Q-dependent susceptibility is shown in figure 5. To perform the integration (5), the spectral weight $\mathrm{Im}\,\chi(Q, \hbar\omega)/\hbar\omega$ was extended above 6 meV by assuming a Lorentzian function $A/[(\hbar\omega)^2 + \Gamma^2]$ with $\Gamma \simeq 4$ meV. A simple extrapolation of the uniform susceptibility [3] to finite Q, $(\chi_\alpha + \chi_\beta)f(Q)^2$, where $f(Q)$ is a form factor of Ce^{3+} [20], is also plotted in figure 5. This extrapolation is based upon two assumptions: the magnetic moment operator can be represented by the dipole approximation

$$M_Q^\alpha \simeq -g\mu_B f(Q) \sum_r \exp(-iQ \cdot r) J_r^\alpha \tag{8}$$

where J_r^α is the angular momentum operator of the $J = \frac{5}{2}$ multiplet; there is no magnetic correlation between different sites, $\langle J_r^\alpha J_{r'}^\alpha \rangle = 0$, which is reasonable for the single-site contribution.

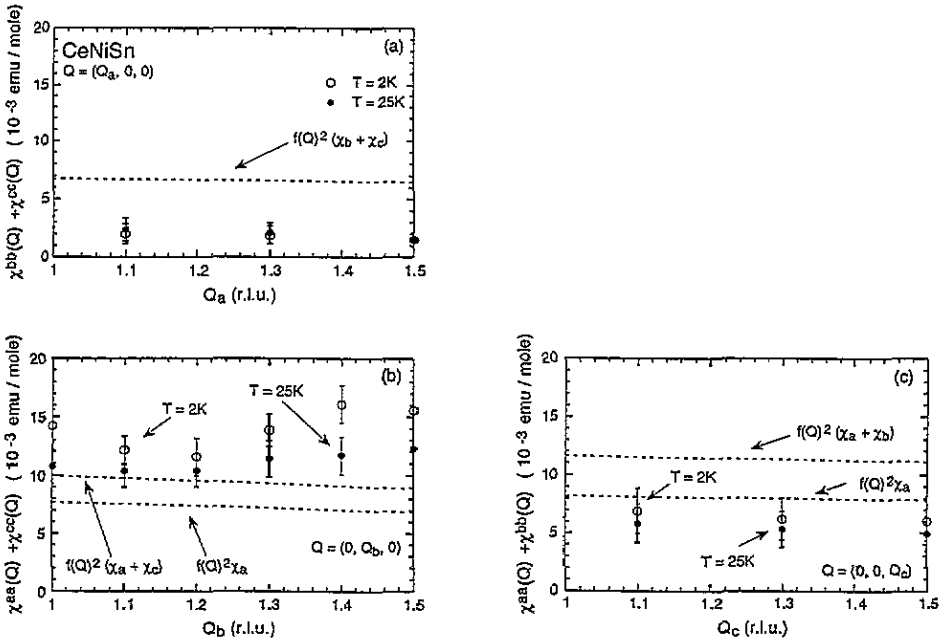

Figure 5. The wave-number-dependent susceptibility calculated by applying the Kramers–Kronig relation (5) to the constant-Q scan shown in figures 2, 3 and 4: (a) $\chi^{bb}(Q)+\chi^{cc}(Q)$ for the scan on the a^*-axis; (b) $\chi^{cc}(Q)+\chi^{aa}(Q)$ for the scan on the b^*-axis; (c) $\chi^{aa}(Q)+\chi^{bb}(Q)$ for the scan on the c^*-axis. The open and closed circles denote data at $T = 2$ and 25 K, respectively. To perform the integration (5), we extrapolated the constant-Q spectrum above 6 meV using the Lorentzian spectral weight. The broken line is the simple extrapolation of uniform susceptibility to finite Q, that is, $f(Q)^2(\chi_\alpha + \chi_\beta)$ or $f(Q)^2\chi_\alpha$ ($\alpha = x, y, z$), where χ_α is the measured uniform susceptibility [3] and $f(Q)$ is the Ce^{3+} form factor.

Figure 5(a) clearly shows that the Q-dependent susceptibility $\chi^{bb}(Q) + \chi^{cc}(Q)$ falls considerably short of the uniform susceptibility. This implies that the assumption of the Lorentzian above 6 meV is not correct in the integration (5), that is, there are larger spectral weights above 6 meV for $\mathrm{Im}\,\chi^{bb}(Q, \hbar\omega)$ and $\mathrm{Im}\,\chi^{cc}(Q, \hbar\omega)$. These spectral weights suggest the presence of crystal field excitations in the high-energy region. Since the calculated $\chi^{bb}(Q)$ and $\chi^{cc}(Q)$ are quite small, the data points shown in figures 5(b) and 5(c) can be mainly attributed to $\chi^{aa}(Q)$. They are Q dependent along the b^*-axis and show appreciable anisotropy in the Q space, i.e., $\chi^{aa}(0, Q_b, 0) > \chi^{aa}(0, 0, Q_c)$. If the Q dependence is averaged, the magnitude of the calculated $\chi^{aa}(Q)$ is consistent with the uniform susceptibility $f(Q)^2\chi_a$, which is also shown in figure 5(b) and (c). This consistency leads us to conclude that the spectral weight of $\mathrm{Im}\,\chi^{aa}(Q, \hbar\omega)/\hbar\omega$ is localized in the quasi-elastic energy range. We note that it also gives confidence in the procedure for estimating the non-magnetic background.

These experimental results can be expressed in terms of the crystal field splitting. Matrix elements of J_τ^a in the ground doublet, which becomes the excitation continuum if the hybridization sets in, give the dominant contribution to $\mathrm{Im}\,\chi^{aa}(Q, \hbar\omega)$. On the other hand, matrix elements of J_τ^b and J_τ^c, which determine $\mathrm{Im}\,\chi^{bb}(Q, \hbar\omega)$ and $\mathrm{Im}\,\chi^{cc}(Q, \hbar\omega)$, are much smaller in the ground doublet and should be large between the ground and excited doublets.

3.3. 2 meV excitation

The 2 meV excitation was reported in detail in [15]. A constant-Q scan shows a pseudogap spectral weight at $Q = (0, 0, 1)$, with a peak at 2 meV. The excitation peak develops below 15 K, which is in accord with T_{coh}. Although the peak energy does not depend on Q, the spectra lose intensity and become broadened when Q departs from (0,0,1). We confirmed this excitation by a constant-Q scan at $Q = (0, 0, 1.1)$ as shown in figure 4(c). However, it should be noted that the pseudogap-type spectrum was not confirmed in the present study, because the energy resolution of the scans of the present study, which is 0.9 meV (FWHM), is much larger than that of [15], being 0.25 meV (FWHM). A new finding of the present experiment is the fact that the 2 meV excitation also appears at $Q = (0, 1, 0)$, which is shown in figure 3(f). It clearly shows temperature dependence. Since $Q = (0, 0, 1)$ and $(0, 1, 0)$ are forbidden nuclear reflections, the 2 meV excitation can be regarded as dynamic antiferromagnetic correlation along the a-axis. We note that antiferromagnetic orders that produce $(0, 0, 1)$ and $(0, 1, 0)$ reflections are such that the magnetic unit cell coincides with that of the lattice structure, and that the four moments in the unit cell are anti-parallel. A possible antiferromagnetic spin arrangement will be discussed in section 4.

3.4. 4 meV excitation

The most remarkable feature of the constant-Q scans on the a^*-, b^*- and c^*-axes, shown in figures 2, 3 and 4, is the pronounced peak at $\hbar\omega = 4$ meV and $Q = (0, \frac{3}{2}, 0)$. The temperature dependence of the spectrum is shown in figure 3(a). The peak intensity at $\hbar\omega = 4.25$ meV is plotted as a function of temperature in figure 6. The 4 meV peak develops gradually below 20 K, which is associated with T_{coh}.

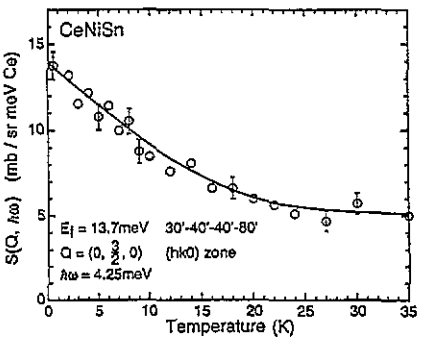

Figure 6. The temperature dependence of peak intensity of the 4 meV excitation taken at $Q = (0, \frac{3}{2}, 0)$ and $\hbar\omega = 4.25$ meV. The solid line is a guide to the eye.

Above 20 K the spectrum does not show much structure. The spectral weight at $T = 2$ K shows a pseudogap-type spectrum which loses weight below 3 meV.

To investigate the Q dependence of the 4 meV excitation, we performed a number of constant-Q scans. The 4 meV excitation peak was observed in any constant-Q scan at $Q = (Q_a, \frac{1}{2} + n, Q_c)$, where n is an integer. It should be noted that the modulation $k = (0, \frac{1}{2}, 0)$ is close to the modulation vectors of antiferromagnetic structures in the isostructural compounds CePtSn and CePdSn [21]. Several constant-Q scans in the $(0, k, l)$, $(h, k, 0)$ and (h, k, h) scattering planes are shown in figures 7, 8 and 9, respectively. These spectra are essentially the same as that at $Q = (0, \frac{3}{2}, 0)$. This Q dependence strongly suggests that the 4 meV excitation depends on neither Q_a nor Q_c, that is, the excitation is quasi-one-dimensional along the b-axis. The spectrum at $Q = (2, \frac{1}{2}, 0)$ (see figure 10) is much smaller than that at $Q = (0, \frac{3}{2}, 0)$. This indicates that the 4 meV excitation is

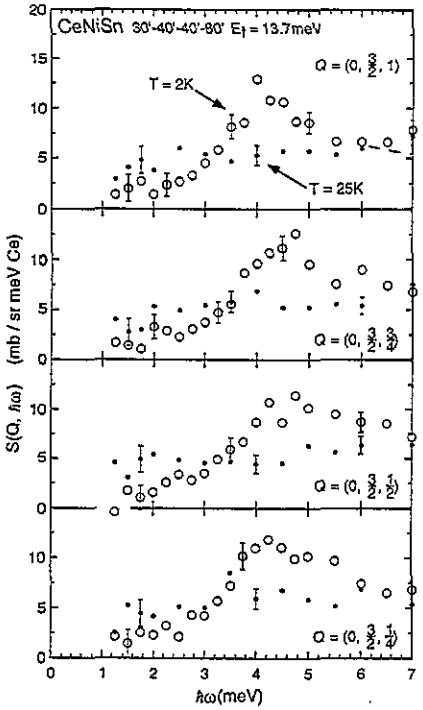

Figure 7. The constant-Q scan at $Q = (0, \frac{3}{2}, Q_c)$, $Q_c = 1, \frac{3}{4}, \frac{1}{2}$ and $\frac{1}{4}$. The open and closed circles denote data at $T = 2$ and 25 K, respectively. The broken line stands for phonon-subtracted magnetic contribution.

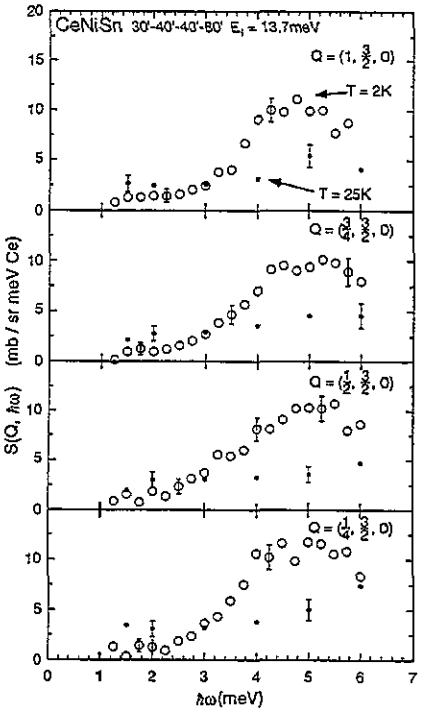

Figure 8. The constant-Q scan at $Q = (Q_a, \frac{3}{2}, 0)$, $Q_a = 1, \frac{3}{4}, \frac{1}{2}$ and $\frac{1}{4}$. The open and closed circles denote data at $T = 2$ and 25 K, respectively.

attributable to Im $\chi^{aa}(Q, \hbar\omega)$, in agreement with the discussion in section 3.2. When Q_b departs from $\frac{3}{2}$ (see spectra at $Q = (0, 1.4, 0)$ and $(0, 1.3, 0)$ in figures 3(b) and 3(c)) the 4 meV excitation becomes broadened and weak. These results lead us to conclude that the 4 meV excitation is not a mode such as crystal field excitations, but should be regarded as dynamic antiferromagnetic correlation characterizing the Kondo coherent state of CeNiSn.

To confirm the quasi-one-dimensional character and the anisotropy of Im $\chi^{\alpha\alpha}(Q, \hbar\omega)$, we performed constant-$E$ scans at $\hbar\omega = 4.25$ meV in a wide range of Q-space through $(0,\frac{1}{2},0)$, $(0,\frac{3}{2},0)$ and $(0, \frac{1}{2}, 1)$ along the a^*-, b^*- and c^*-directions at $T = 2$ and 25 K. We examined a wide Q-range, because Im $\chi^{\alpha\beta}(Q, \hbar\omega)$ is not necessarily a periodic function with periods a^*, b^* and c^*, which will be discussed in section 4. Spectra of the constant-E scans are shown in figure 11. Scans along Q_b (figure 11(a)) show peaks at $Q_b = \frac{1}{2}$ and $\frac{3}{2}$. The width of the peak $\Delta Q_b = 0.2\ b^*$ (HWHM) corresponds to a short correlation length $\xi_b = 1/(2\pi\Delta Q_b) = 0.8b$. On the other hand, $S(Q, \hbar\omega)$ of the scan along $(0, \frac{1}{2}, Q_c)$ (figure 11(b)) is almost constant except for a small periodic modulation. $S(Q, \hbar\omega)$ along $(Q_a, \frac{1}{2}, 0)$ and $(Q_a, \frac{3}{2}, 0)$ (figures 11(c) and 11(d)) decreases with increasing Q_a. It also exhibits a small periodic modulation. Those small modulations suggest the existence of weak three-dimensional correlations. If the small modulations are neglected, one finds that the variation of $S(Q, \hbar\omega)$ along the c^*-direction is well approximated by the form

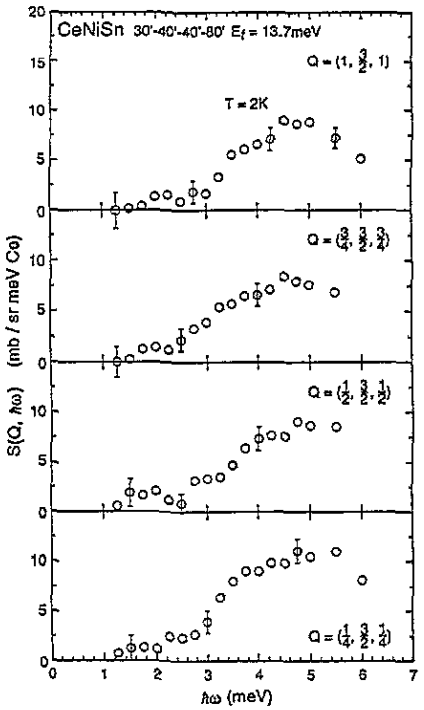

Figure 9. The constant-Q scan at $T = 2$ K and $Q = (Q_a, \frac{3}{2}, Q_c)$, $Q_a = Q_c = 1, \frac{3}{4}, \frac{1}{2}$ and $\frac{1}{4}$.

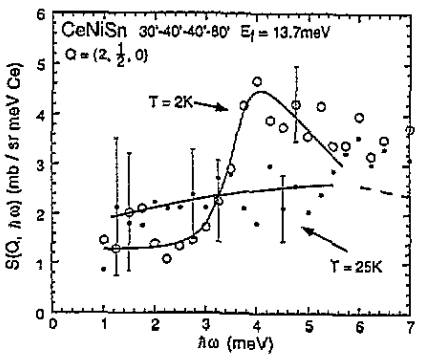

Figure 10. The constant-Q scan at $Q = (2, \frac{1}{2}, 0)$. The open and closed circles denote data at $T = 2$ and 25 K, respectively. The solid and broken lines are a guide to the eye and phonon-subtracted magnetic contribution, respectively.

factor $f(Q)^2$, whereas $S(Q, \hbar\omega)$ along the a^*-direction by the orientational factor of $\mathrm{Im}\,\chi^{aa}(Q, \hbar\omega)$ and the form factor, that is, $(1 - \hat{Q}_a^2) f(Q)^2$. Those approximate functions are shown by the dashed-and-dotted and broken lines in the figures. In the scan along the a^*-direction, deviation from $(1 - \hat{Q}_a^2) f(Q)^2$ is seen for $Q_a > 2$. In fact, a constant-Q scan at $Q = (2, \frac{1}{2}, 0)$ (figure 10) shows a small but finite peak at $\hbar\omega = 4$ meV. It comes from contributions of $\mathrm{Im}\,\chi^{bb}(Q, \hbar\omega)$, $\mathrm{Im}\,\chi^{cc}(Q, \hbar\omega)$ and $[\mathrm{Im}\,\chi^{ab}(Q, \hbar\omega) + \mathrm{Im}\,\chi^{ba}(Q, \hbar\omega)]$. By neglecting the small modulations and the deviation at large Q_a as a zero-order approximation, we conclude that the 4 meV excitation has three characteristics. (1) It is quasi-one-dimensional. (2) It is mainly attributed to magnetic fluctuation along the a-axis, $\mathrm{Im}\,\chi^{aa}(Q, \hbar\omega)$. (3) $\mathrm{Im}\,\chi^{aa}(Q, \hbar\omega)$ is a periodic function with periods a^*, b^* and c^*. Real-space antiferromagnetic correlation associated with the 4 meV excitation will be discussed in section 4.

The appearance of the weak three-dimensional character of $S(Q, \hbar\omega)$ of the 4 meV excitation depends on the energy resolution of the experiment. This was pointed out by a recent report of Mason *et al* [22]. They performed experiments with a high resolution and clearly showed three-dimensional modulation of the 4 meV excitation. To see the origin of this modulation, we carried out a constant-E and two constant-Q scans with a high resolution of 0.4 meV (FWHM) at $\hbar\omega = 4$ meV, which is about one-third of the low resolution of 1.1 meV (FWHM) of the spectra in figures 3, 7, 9, 10, 11, 14 and 15. A high-resolution

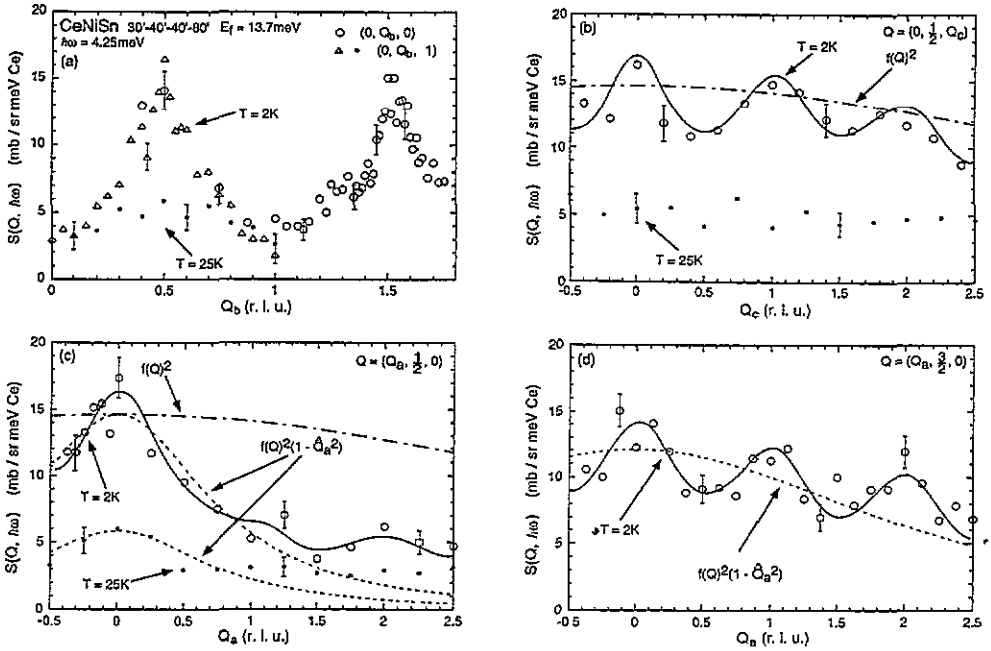

Figure 11. Constant-E scan at $\hbar\omega = 4.25$ meV through $(0, \frac{1}{2}, 0)$, $(0, \frac{3}{2}, 0)$ or $(0, \frac{1}{2}, 1)$. (a) Scan along $Q = (0, Q_b, 0)$ (open circle) and $Q = (0, Q_b, 1)$ (triangle and closed circle). (b) Scan along $Q = (0, \frac{1}{2}, Q_c)$. (c) Scan along $Q = (Q_a, \frac{1}{2}, 0)$. (d) Scan along $Q = (Q_a, \frac{3}{2}, 0)$. The open circle and triangle denote data at $T = 2$ K, whereas the closed circle stands for data at $T = 25$ K. Dashed-and-dotted and broken lines stand for $f(Q)^2$ and $f(Q)^2(1 - \hat{Q}_a^2)$, respectively, where $f(Q)$ is Ce^{3+} form factor. The solid line is a guide to the eye.

constant-E scan at $\hbar\omega = 4$ meV along $Q = (0, \frac{1}{2}, Q_c)$ is shown in figure 12. It clearly shows the periodic modulation of $S(Q, \hbar\omega)$ with period c^*, which is rather ambiguous in the low-resolution data shown in figure 11(b). Figure 13 shows the constant-Q spectra taken at $Q = (0, \frac{1}{2}, 0)$ and $(0, \frac{1}{2}, \frac{1}{2})$, which correspond to the maximum and minimum of the constant-E scan of figure 12. By comparing them with the low-resolution spectra in figures 3(a) and 7, it is evident that the high-resolution spectrum exhibits a sharper spectral shape, smaller weight below 3 meV and sharp cut-off below the peak. One also sees that the peak energy depends on Q; the peaks are at $\hbar\omega = 4.0$ and 4.7 meV for $Q = (0, \frac{1}{2}, 0)$ and $(0, \frac{1}{2}, \frac{1}{2})$, respectively. This slight Q-dependence of the peak energy is the origin of the modulation of the constant-E scan. Note that except for the slight Q-dependence, the general features of the excitation spectra in the constant-Q scans do not depend on Q_c. Thus we conclude that the quasi-one-dimensionality found by the low-resolution scans is essentially correct, although we have not carried out extensive measurements with the high resolution.

3.5. Spectra for general Q

Finally we show results of several constant-Q scans at general Q-vectors. Spectra at $Q = (0, 1.3, Q_c)$ and $(Q_a, 1.3, 0)$, where Q_a, $Q_c = \frac{1}{4}, \frac{1}{2}, \frac{3}{4}$ and 1, are shown in figures 14 and 15. For the c^*-direction, all the spectra at $T = 2$ K $< T_{coh}$ exhibit a weak and broadened 4 meV peak, which cannot be seen in the spectra at $T = 25$ K $> T_{coh}$. On the other hand, for the spectra along the a^*-direction, the weak and broadened 4 meV peak

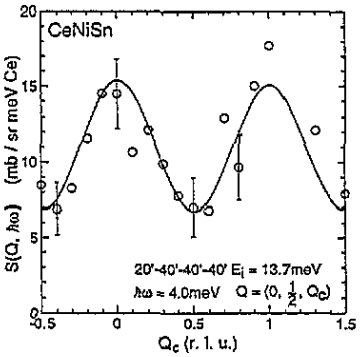

Figure 12. Constant-E scan at $T = 2$ K and $\hbar\omega = 4$ meV along $Q = (0, \frac{1}{2}, Q_c)$ with the high resolution of 0.4 meV (FWHM). The solid line is a guide to the eye.

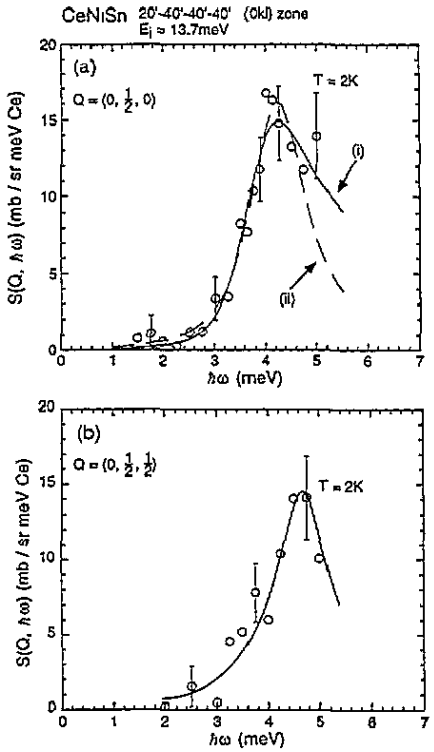

Figure 13. Constant-Q scan with the high resolution of 0.4 meV (FWHM) at $\hbar\omega = 4$ meV. (a) Spectrum at $Q = (0, \frac{1}{2}, 0)$ and $T = 2$ K. The solid and dashed lines are fits to the spectral weight function of equation (14) and the inelastic Lorentzian function (15), respectively. (b) Spectrum at $Q = (0, \frac{1}{2}, \frac{1}{2})$ and $T = 2$ K. The solid line is a guide to the eye.

can be observed at small Q_a. It disappears at large Q_a as $Q_a = 1$, where the spectra are structureless and do not show a temperature difference. This Q-dependence reflects the fact that the spin fluctuation is almost restricted along the a-axis. Shown in figure 16 are constant-Q spectra at $Q = (0, 1, Q_c)$, where $Q_c = \frac{1}{4}, \frac{1}{2}$, and $\frac{3}{4}$. These spectra are also structureless, except for the 2 meV excitation for $Q_c = \frac{1}{4}$, which is reminiscent of the peak at $Q = (0, 1, 0)$.

4. Discussion

In this study, we have measured and presented a number of constant-Q spectra to reveal the overall features of magnetic excitation of CeNiSn. To date, there exists no theoretical work which accounts for the pseudogap behaviour on the basis of a microscopic model calculation. We hence have not performed any serious quantitative analysis, but have shown all data in the absolute scale for the convenience of a future analysis. Accordingly, in this section we will further discuss the excitation spectra solely from an experimental viewpoint.

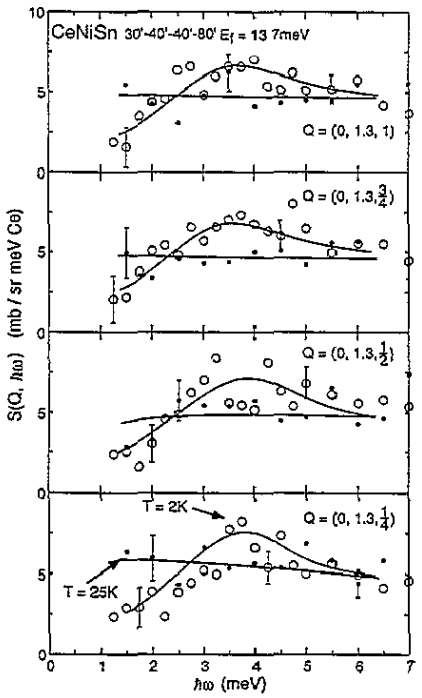

Figure 14. Constant-Q scan at $Q = (0, 1.3, Q_c)$, $Q_c = 1, \frac{3}{4}, \frac{1}{2}$ and $\frac{1}{4}$. The open and closed circles stand for data at $T = 2$ K and 25 K, respectively. The solid line is a guide to the eye.

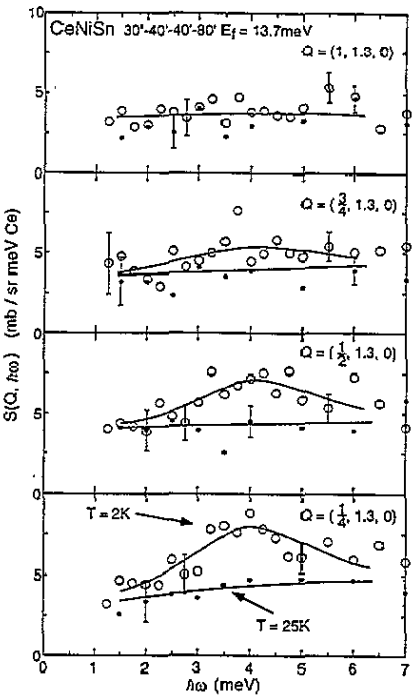

Figure 15. Constant-Q scan at $Q = (Q_a, 1.3, 0)$, $Q_a = 1, \frac{3}{4}, \frac{1}{2}$ and $\frac{1}{4}$. The open and closed circles stand for data at $T = 2$ K and 25 K, respectively. The solid line is a guide to the eye.

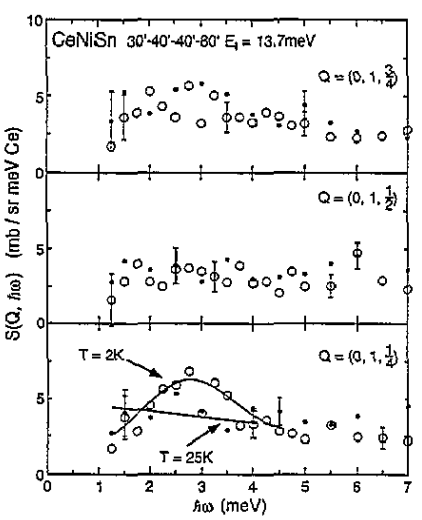

Figure 16. Constant-Q scan at $Q = (0, 1, Q_c)$, $Q_c = \frac{3}{4}, \frac{1}{2}$ and $\frac{1}{4}$. The open and closed circles stand for data at $T = 2$ K and 25 K, respectively. The solid line is a guide to the eye.

4.1. Crystal field

Although the crystal field splitting has not been determined, it definitely affects the anisotropy of the magnetic susceptibility and temperature dependence of the resistivity,

and should be clarified for the microscopic understanding of CeNiSn. The anisotropy of magnetic fluctuation discussed in section 3.2 shows that the easy axis is along the a-axis. This easy axis has been thought to be brought about by the structural property in which Ce atoms, surrounded by distorted hexagonal prisms of Ni and Sn, form zigzag chains along the a-axis [2, 3]. Along this line, Alekseev *et al* [13] proposed that the crystal field approximately follows trigonal symmetry D_{3h} where the a-axis is the symmetry axis, and that three doublets are $|\pm\frac{3}{2}\rangle$, $(a\,|\pm\frac{1}{2}\rangle + b\,|\mp\frac{5}{2}\rangle)$ and $(-b\,|\pm\frac{1}{2}\rangle + a\,|\mp\frac{5}{2}\rangle)$. The experimental results of section 3.2 show that the matrix elements of J_r^a within the ground doublet are much larger than those of J_r^b and J_r^c. This indicates that the ground doublet is either $|\pm\frac{3}{2}\rangle$ or $(a\,|\pm\frac{1}{2}\rangle + b\,|\mp\frac{5}{2}\rangle)$ with $|b| \gg |a|$. Further study is required to distinguish between $|\pm\frac{3}{2}\rangle$ and $|\pm\frac{5}{2}\rangle$.

4.2. Real-space spin configuration of antiferromagnetic correlation

The Q-dependence of the scattering intensity of the 2 and 4 meV excitations provides information on the real-space spin configuration of the corresponding dynamic antiferromagnetic correlations. Within the dipole approximation (8), the pair correlation function is approximated by

$$\langle M_Q^a M_{-Q}^a(t)\rangle \propto (f(Q))^2 \sum_{\mu\mu'} \sum_{RR'} \exp[-\mathrm{i}Q\cdot(d_\mu - d_{\mu'}) - \mathrm{i}Q\cdot(R-R')] \times \langle J_{d_\mu+R}^a J_{d_{\mu'}+R'}^a(t)\rangle \tag{9}$$

where R (R') and d_μ ($d_{\mu'}$) are positions of the unit cell and Ce sites in the unit cell, respectively: $R = n_a a + n_b b + n_c c$, where n_a, n_b and n_c are integers; $d_\mu = xa + yb + zc$, where $0 \leqslant x, y, z < 1$. There are four Ce sites in the unit cell, and their positions d_μ are indexed by μ ($\mu = 1, 2, 3, 4$) as shown in figure 17. We note that $\langle M_Q^a M_{-Q}^a(t)\rangle$ is generally incommensurate in the reciprocal lattice space because of the phase factor $\exp[-\mathrm{i}Q\cdot(d_\mu - d_{\mu'})]$ in (9). This is the reason why we examined the constant-E scans in a wide Q-range.

There are two dynamic antiferromagnetic correlations with different frequencies $\hbar\omega_2 = 2$ and $\hbar\omega_4 = 4$ meV. Since they have different Q-dependence, we discuss the real-space spin configurations of the two correlations separately.

As discussed in section 3.4, the dynamic antiferromagnetic correlation with $\hbar\omega_4$ has two features: quasi-one dimensional and periodic in the reciprocal lattice space. The periodicity is satisfied by a requirement on the spin correlation

$$\langle J_{d_\mu+R}^a J_{d_{\mu'}+R'}^a(t)\rangle = 0 \quad \text{for} \quad \mu \neq \mu'. \tag{10}$$

The quasi-one-dimensional Q-dependence along the b-axis implies

$$\langle J_{d_\mu+R}^a J_{d_\mu+R'}^a(t)\rangle \begin{cases} = 0 & \text{for } R' \neq R + nb \\ \propto (-1)^n \exp[-|n|b/\xi_b]\exp[\mathrm{i}\omega_4 t] & \text{for } R' = R + nb. \end{cases} \tag{11}$$

The real-space spin configuration of the correlation (10) and (11) is schematically depicted in figure 17(a).

As shown in section 3.3, the 2 meV excitation appears at $Q = (0, 0, 1)$ and $(0, 1, 0)$. To uniquely determine the spin configuration of this antiferromagnetic correlation, more data at equivalent Q-vector are required. Hence we will just show the simplest spin configuration which is compatible with the experiment. Since $(0, 0, 1)$ and $(0, 1, 0)$ are forbidden nuclear reflections, we consider a short-range order of a collinear antiferromagnetic order which has the same unit cell as the crystal structure and zero total moment within the

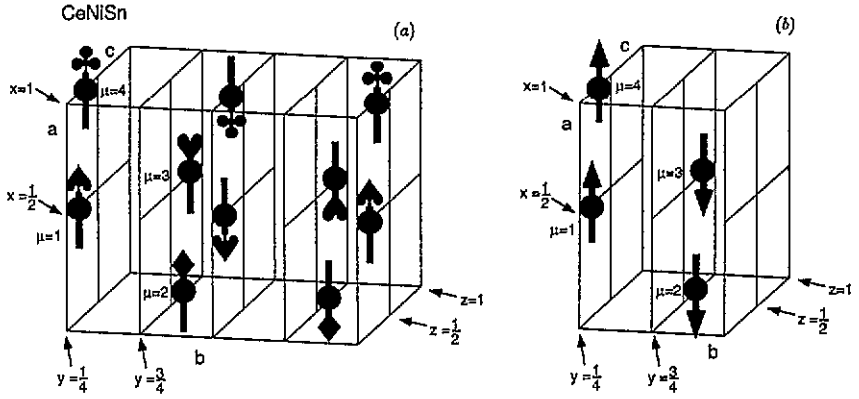

Figure 17. Schematic illustration of real-space antiferromagnetic correlations of the 4(a) and 2(b) meV excitations. Several near-neighbouring magnetic moments which characterize the short-range order are drawn as arrows. Closed circle stands for four Ce positions d_μ in unit cell: $d_1 = (x, \frac{1}{4}, z)$, $d_2 = (\bar{x} + \frac{1}{2}, \frac{3}{4}, z + \frac{1}{2})$, $d_3 = (\bar{x} + 1, \frac{3}{4}, \bar{z} + 1)$ and $d_4 = (x + \frac{1}{2}, \frac{1}{4}, \bar{z} + \frac{1}{2})$ ($x = 0.48$, $y = 0.20$). (a) The short-range order of the 4 meV excitation expressed by equations (10) and (11) is represented by four kinds of arrow. Moments of the same arrow couple antiferromagnetically along the b-axis. Moments of the different arrows have no correlation to each other. (b) The short-range order of the 2 meV excitation expressed by equation (12) and $(\sigma_{d_1}, \sigma_{d_2}, \sigma_{d_3}, \sigma_{d_4}) = (1, -1, -1, 1)$. Moments in unit cell are drawn.

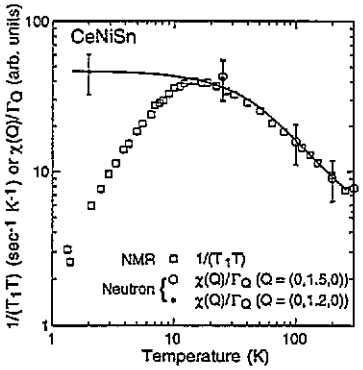

Figure 18. Comparison of spin excitation at $\hbar\omega = 0$ between observation of $1/T_1$ by NMR experiment [11] and extrapolation of $S(Q, \hbar\omega \to 0)$ from $\hbar\omega > 1$ meV by neutron scattering. $1/(T_1T)$ and $S(Q, \hbar\omega \to 0)/T \propto \chi(Q)/\Gamma_Q$ are plotted as a function of temperature. For neutron scattering, representative data at $Q = (0, \frac{3}{2}, 0)$ ($25 \leqslant T \leqslant 300$ K) and $Q = (0, 1.2, 0)$ ($2 \leqslant T \leqslant 25$ K) are used.

unit cell. There are three independent antiferromagnetic configurations in the unit cell: $(\sigma_{d_1}, \sigma_{d_2}, \sigma_{d_3}, \sigma_{d_4}) = (1, 1, -1, -1), (1, -1, -1, 1), (1, -1, 1, -1)$, where $\sigma_{d_\mu} \propto J^a_{d_\mu}$. If the spin correlation is assumed to be expressed by

$$\langle J^a_{d_\mu + R} J^a_{d_{\mu'} + R'}(t) \rangle \propto \sigma_{d_\mu} \sigma_{d_{\mu'}} \exp[|R - R'|\kappa] \exp[i\omega_2 t] \tag{12}$$

$\langle M^a_Q M^a_{-Q}(t) \rangle$ becomes

$$\langle M^a_Q M^a_{-Q}(t) \rangle \propto (f(Q))^2 |F_M(Q)|^2 \frac{1}{\kappa^2 + q^2} \exp[i\omega_2 t] \tag{13}$$

$$F_M(Q) = \sum_{\mu} e^{iQ\cdot d_\mu}\sigma_{d_\mu}$$

where $q = |Q-G|$ and $G = (0, 0, 1)$ or $(0, 1, 0)$. Thus the scattering intensity is determined by $(f(Q))^2|F_M(Q)|^2$. We calculated $(f(Q))^2|F_M(Q)|^2$ at $Q = (0, 0, 1)$ and $(0, 1, 0)$ for the three configurations. They are $((f(0,0,1))^2|F_M(0,0,1)|^2, (f(0,1,0))^2|F_M(0,1,0)|^2) = (0, 0)$, $(13.8, 14.5)$ and $(1.6, 0)$ for $(\sigma_{d_1}, \sigma_{d_2}, \sigma_{d_3}, \sigma_{d_4}) = (1, 1, -1, -1)$, $(1, -1, -1, 1)$ and $(1, -1, 1, -1)$, respectively. It is evident that the intensities of the 2 meV excitation observed at $Q = (0, 0, 1)$ and $(0, 1, 0)$ agree only with the $(1, -1, -1, 1)$ configuration, which is illustrated in figure 17(b).

4.3. Spectral weight function

The inelastic peaks appearing at $\hbar\omega = 2$ and 4 meV show the pseudogap-type spectra. The spectral weight function of the 2 meV excitation is well discussed by Mason *et al* [15]. Thus we have attempted to fit the spectral weight only for the 4 meV excitation. The following two functions are used for the fitting:

$$\frac{\mathrm{Im}\,\chi(Q,\hbar\omega)}{\hbar\omega} \propto |\epsilon|\left(\mathrm{Re}\left(\frac{1}{\sqrt{(\hbar\omega)^2-\epsilon^2}}\right)\right)^2 \qquad \epsilon = \Delta + i\Gamma_1 \tag{14}$$

$$\frac{\mathrm{Im}\,\chi(Q,\hbar\omega)}{\hbar\omega} \propto \left(\frac{\Gamma_2}{\Gamma_2^2+(\hbar\omega-\hbar\omega_0)^2} + \frac{\Gamma_2}{\Gamma_2^2+(\hbar\omega+\hbar\omega_0)^2}\right). \tag{15}$$

Equation (14) was used in [15] for the asymmetric spectra of the 2 meV excitation, whereas the Lorentzian with a finite peak energy (15) has been adopted for the quasi-elastic scattering of several heavy-fermion and valence-fluctuation compounds [23]. We fitted the constant-Q scan at $Q = (0, \frac{1}{2}, 0)$ and $T = 2$ K to the resolution-convoluted $S(Q, \hbar\omega)$ based on (14) and (15). The fitted curves are shown in figure 13(a) by the solid (function (14)) and dashed (function (15)) lines. The observed spectrum is well approximated by both the functions except for the slight asymmetry, which can be reproduced only by function (14). The optimum parameters are $\Delta = 3.8 \pm 0.1$ meV, $\Gamma_1 = 0.7 \pm 0.14$ meV; $\hbar\omega_0 = 4.2 \pm 0.6$ meV, $\Gamma_2 = 0.6 \pm 0.1$ meV.

4.4. Pseudogap of the order T_Δ

The pseudogap in the magnetic excitation of the order T_Δ is most beautifully exhibited in the temperature dependence of $1/T_1 \propto T^3$, observed in the NMR experiment [10, 11]. In a crude approximation, $1/T_1$ is related to the magnetic fluctuation at $\hbar\omega \to 0$ [24], more specifically;

$$\frac{1}{T_1} \propto \sum_Q S(Q, \hbar\omega \to 0) \propto \sum_Q \left[\frac{\mathrm{Im}\,\chi(Q,\hbar\omega)}{\beta\hbar\omega}\right]_{\hbar\omega\to 0}. \tag{16}$$

Thus we can check the consistency between the NMR and neutron experiments. This comparison also enables us to guess the form of the spectral weight for the pseudogap of the order T_Δ. If the spectral weight can be approximated by a Lorentzian, then one has

$$\frac{\mathrm{Im}\,\chi(Q,\hbar\omega)}{\hbar\omega} \propto \chi(Q)\frac{\Gamma_Q}{(\hbar\omega)^2+\Gamma_Q^2}. \tag{17}$$

Extrapolated to $\hbar\omega \to 0$, equations (16) and (17) provide a relation

$$\frac{1}{T_1 T} \propto \sum_Q \chi(Q)\frac{1}{\Gamma_Q}. \tag{18}$$

To obtain the temperature dependence of the right-hand side of equation (18), it is sufficient to replace the summation with one term $\chi(Q)/\Gamma_Q$ at a representative Q where the spectrum shows only the quasi-elastic features. We used the spectra at $Q = (0, 1.2, 0)$ for $2 \leqslant T \leqslant 25$ K and at $(0, 1.5, 0)$ for $25 \leqslant T \leqslant 300$ K. These data were fitted to the Lorentzian (17). Figure 3(d) shows the result of the fitting for the spectrum at $Q = (0, 1.2, 0)$ and $T = 2$ K. The spectrum is well approximated by the Lorentzian, shown by the dashed-and-dotted line in the figure. The temperature dependences of $\chi(Q)/\Gamma_Q$ and $1/(T_1T)$ are plotted in figure 18. One can see that the NMR and neutron scattering agree well above 10 K. However, they show remarkable difference below 10 K, which implies that the Lorentzian form of the spectral weight, equation (17), is not applicable for the extrapolation $\hbar\omega \to 0$ in (16). The strong decrease of $1/(T_1T)$ at $T \ll T_\Delta$ indicates that $\sum_Q [\mathrm{Im}\,\chi(Q, \hbar\omega)/\hbar\omega]_{\hbar\omega\to 0}$ vanishes at $T = 0$. Therefore, if the Q-dependence is neglected, we can expect at $T \ll T_\Delta$

$$\mathrm{Im}\frac{\chi(Q,\hbar\omega)}{\hbar\omega} \propto \begin{cases} \chi(Q)\dfrac{\Gamma_Q}{(\hbar\omega)^2+\Gamma_Q^2} & \text{for } \hbar\omega \gg k_B T_\Delta \\ (\hbar\omega)^2 & \text{for } \hbar\omega \ll k_B T_\Delta \end{cases} \tag{19}$$

as the pseudogap spectral weight. Thus we think the pseudogap behaviour in the energy range $\hbar\omega < k_B T_\Delta$ remains to be studied with a higher energy resolution.

5. Conclusions

The spin excitations in CeNiSn were investigated in the wide Q-range and in the energy range of $\hbar\omega = 1.2$–7 meV by means of neutron scattering. The magnetic fluctuation at low temperatures in this energy range is dominated by the easy a-axis component $\mathrm{Im}\,\chi^{aa}$. Below the onset temperature of Kondo coherence, $T_{\mathrm{coh}} = 12$–20 K, two dynamic antiferromagnetic correlations develop as excitation peaks at $\hbar\omega = 2$ and 4 meV at the special Q-positions, whereas at general Q-positions the spectra are quasi-elastic and do not show a difference between above and below T_{coh}. The 4 meV excitation appears at $Q = (Q_a, \frac{1}{2}+n, Q_c)$ where Q_a and Q_c are arbitrary and n is an integer. The Q-dependence shows that the antiferromagnetic correlation is quasi-one dimensional along the b-axis. The 2 meV excitation appears around $Q = (0, 0, 1)$ and $(0, 1, 0)$, and its Q-dependence is three dimensional. Unique features of these excitations, as compared to other metallic Kondo compounds, are the pseudogap-type spectral weight at the special Q-positions in which spectra lose weight rapidly below the excitation peaks. We think that the 2 and 4 meV excitations reflect the nature of the Kondo coherence in CeNiSn. The magnetic excitation can exhibit another pseudogap-type spectrum in a wider Q-range in the pseudogap energy scale of $k_B T_\Delta = 0.6$ meV. Thus the low-energy magnetic excitation remains to be studied with a higher energy resolution.

Acknowledgments

The authors would like to thank Y Kitaoka, M Kohgi, K Miyake and S Takagi for valuable discussions. One of the authors (TT) acknowledges the support of the Yamada Science Foundation.

References

[1] Fisk Z, Canfield P C, Thompson J D and Hundley M F 1992 *J. Alloys. Compounds* **181** 369
Millis A 1992 *Physical Phenomena at High Magnetic Fields* ed E Manousakis *et al* (Redwood City: Addison-Wesley)
Aeppli G and Fisk Z 1992 *Comments Condens. Mater Phys.* **16** 155

[2] Takabatake T, Nakazawa Y and Ishikawa M 1987 *Japan. J. Appl. Phys. Suppl.* 3 **26** 547
Takabatake T, Teshima F, Fujii H, Nishigori S, Suzuki T, Fujita T, Yamaguchi Y, Sakurai J and Jaccard D 1990 *Phys. Rev.* B **41** 9607
Takabatake T and Fujii H 1993 *Japan. J. Appl. Phys.* **8** 254

[3] Takabatake T, Nakamoto G, Tanaka H, Bando Y, Fujii H, Nishigori S, Goshima H, Suzuki T, Fujita T, Oguro I, Hiraoka T and Malik S K 1994 *Physica* B **199 & 200** 457

[4] Malik S K and Adroja D T 1991 *Phys. Rev.* B **43** 6277

[5] Allen J W, Batlogg B and Wachter P 1979 *Phys. Rev.* B **20** 4807

[6] Kasaya M, Iga F, Takigawa M and Kasuya T *1985 J. Magn. Magn. Mater.* **47 & 48** 429

[7] Hundley M F, Canfield P C, Thompson J D, Fisk Z, Lawrence J M 1990 *Phys. Rev.* B **42** 6842
Bucher B, Schlesinger Z, Canfield P C and Fisk Z 1994 *Phys. Rev. Lett.* **72** 522

[8] Higashi I, Kobayashi K, Takabatake T and Kasaya M 1993 *J. Alloys Compounds* **193** 300

[9] Haen P, Flouquet J, Lapierre F and Lejay P 1987 *J. Low Temp. Phys.* **67** 391

[10] Kyogaku M, Kitaoka Y, Nakamura H, Asayama K, Takabatake T, Teshima F and Fujii H 1990 *J. Phys. Soc. Japan* **59** 1728
Kyogaku M, Kitaoka Y, Asayama K, Takabatake T and Fujii H 1992 *J. Phys. Soc. Japan* **61** 43

[11] Nakamura K, Kitaoka Y, Asayama K, Takabatake T, Tanaka H and Fujii H 1994 *J. Phys. Soc. Japan* **63** 433

[12] Alekseev P A, Clementyev E S, Lazukov V N, Sadikov I P, Goremychkin E A and Sashin I L 1993 *Physica* B **186–188** 416

[13] Alekseev P A, Klement'ev E S, Lazukov V N, Nefedova E V, Sadikov I P, Khlopkin M N, Muzychka A Yu, Sashin I L, Efremova N N and Bührer W 1994 *Sov. Phys.–JETP* **79** 665

[14] Kohgi M, Ohoyama K, Osakabe T, Kasaya M, Takabatake T and Fujii H 1993 *Physica* B **186–188** 409

[15] Mason T E, Aeppli G, Ramirez A P, Clausen K N, Broholm C, Stücheli N, Bucher E and Palstra T T M 1992 *Phys. Rev. Lett.* **69** 490

[16] Kadowaki H, Sato T, Yoshizawa H, Ekino T, Takabatake T, Fujii H, Regnault L P and Isikawa Y 1994 *J. Phys. Soc. Japan* **63** 2074

[17] Rossat-Mignod J, Regnault L P, Jacoud J L, Vettier C, Lejay P, Flouquet J, Walker E, Jaccard D and Amato A 1988 *J. Magn. Magn. Matter.* **76 & 77** 376

[18] Isikawa Y, Mori K, Ogisi Y, Oyaba K and Sato K 1991 *J. Phys. Soc. Japan* **60** 2514

[19] Lovesey M 1984 *Theory of Neutron Scattering From Condensed Matter* (Oxford: Clarendon)

[20] Blume M, Freeman A J and Watson R E 1962 *J. Chem. Phys.* **37** 1245

[21] Kadowaki H, Ekino T, Iwasaki H, Takabatake T, Fujii H and Sakurai J 1993 *J. Phys. Soc. Japan* **62** 4426
Kasaya M, Tani T, Suzuki H, Ohoyama K and Kohgi M 1991 *J. Phys. Soc. Japan* **60** 2542
Kadowaki H, Kohgi M, Ohoyama K and Kasaya M 1994 *J. Phys. Soc. Japan* **63** 2337

[22] Mason T E *et al* 1995 *Int. Conf. on Neutron Scattering '94 (Sendai, Japan)*

[23] See e.g.
Loewenhaupt M and Fischer K H 1993 *Handbook on the Physics and Chemistry of Rare Earths* vol 16 (Amsterdam: Elsevier) p 1

[24] Moriya T 1963 *J. Phys. Soc. Japan* **18** 516